This is a repository copy of *Incompressible SPH simulation of wave interaction with porous structure*.

White Rose Research Online URL for this paper:
http://eprints.whiterose.ac.uk/91395/

Version: Accepted Version

eprints@whiterose.ac.uk
https://eprints.whiterose.ac.uk/

Incompressible SPH simulation of wave interaction with porous structure

Qinqin Gui[a], Ping Dong[b], Songdong Shao[c], Yiqiang Chen[d]

[a] Faculty of Maritime and Transportation, Ningbo University, Ningbo, 315211, China. Email: guiqinqin@nbu.edu.cn

[b] Department of Civil Engineering, University of Dundee, Dundee, DD1 4HN, United Kingdom (College of Marine Geosciences, Ocean University of China, Qingdao, 266100, China). Email: p.dong@dundee.ac.uk (Correspondence author)

[c] Department of Civil and Structural Engineering, University of Sheffield, Sheffield, S1 3JD, United Kingdom (State Key Laboratory of Hydraulics and Mountain River Engineering, Sichuan University, Chengdu 610065, China). Email: s.shao@sheffield.ac.uk

[d] Department of Civil Engineering, University of Dundee, Dundee, DD1 4HN, United Kingdom. Email: y.j.chen@dundee.ac.uk

Abstract

In this paper an incompressible Smoothed Particle Hydrodynamics (ISPH) method is applied to investigate the flow motion in and around the porous structure. In order to describe in a simple and effective way the flow through the interface between the porous region and pure fluid region within the SPH framework, a heuristic boundary treatment method has been proposed. The ISPH model is first verified against a theoretical model of wave propagation over a porous bed and then further validated by comparing the predicted wave surface profiles and flow velocity fields with the experiment data for a typical case of flow motion around and inside a submerged porous structure. The good agreement has demonstrated that the improved ISPH model developed in this work is capable of modelling wave interaction with porous structures.

Keyword: ISPH; Porous structure; Porous interface; Wave-structure interaction; Boundary condition.

1 Introduction

Porous structures such as rubble-mound breakwater are widely used to protect coastal infrastructures and beaches from the wave attack. Unlike impermeable structures, the interactions between the waves and porous structure take place both outside and inside of the structure. When reaching the porous structure the waves are usually partially reflected and some of the incoming wave energies dissipate outside the porous structure. However, inside the porous structure, the flow in the pores can induce the friction drag and loss of wave energy and even affect the stability of armour stones. Therefore, an accurate quantification of the flow motion in and around the porous structure is vital to understanding the risks of structure instability under the wave actions.

Sollitt and Cross (1972) developed one of the earliest models for describing the flow through permeable structures by adding the inertial and nonlinear resistance forces into the momentum equations to account for the effect exerted on the porous flow by the solid skeletons. Since then many improved models have been proposed to investigate a wide range of wave propagation problems, including wave transmission, reflection and dissipation around and through arbitrarily-shaped breakwaters with porous layers. These include the models based on the potential flow theory (Sulisz, 1985; Yu and Chwang, 1994), mild-slope equation (Rojanakamthorn et al., 1989) and shallow-water equations (Kobayashi and Wurjanto, 1990; Wurjanto and Kobayashi, 1993). Unfortunately, the predictive capability of these simplified models are very restricted as they are unable to account for some essential flow processes such as the nonlinearity (mild-slope equation), frequency dispersion (shallow-water equation) and wave breaking (potential flow equations).

In recent years, more general and rigorous models have been developed based on van Gent's (1995) Reynolds-averaged Navier-Stokes (RANS) equations, also including those by Huang et al. (2003) and Liu et al. (1999). Huang et al. (2003) coupled the unsteady laminar NS equation model and another NS-type model to separately solve the flows outside and inside the porous structure for a solitary wave interaction with submerged porous breakwater. Liu et al. (1999) derived the RANS equations to study wave overtopping on a breakwater with protective porous armour layer. To solve the governing equations, they employed the resistance force formulas proposed by van Gent (1995) and calibrated the linear coefficient against simple physical experiments, while keeping the inertial and original nonlinear frictional coefficients unchanged. Similarly Hsu et al. (2002) used the Volume-Averaged RANS (VARANS) equations to describe the flow motion around the porous structure, and Karunarathna and Lin (2006) applied their VARANS model to study wave damping over a porous seabed. Garcia et al. (2004) and Lara et al. (2006) used the numerical model of Liu et al. (1999) to investigate wave interactions with a low-crested permeable breakwater and validated their models with the laboratory measurements. Also, the contribution of del Jesus et al. (2012) was to derive a new set of VARANS equations with different turbulence models. Ma et al. (2014) developed a non-hydrostatic model based on the model equation of Hsu et al. (2002), and Wu et al. (2014) proposed a 3-D Large Eddy Simulation (LES) model for the porous flows based on the model equation of Hu et al. (2012). One of the major differences among these models is the use of different turbulence closure models.

All of the above-mentioned models are based on the Eulerian approach. In situations with large free surface deformation, it requires an explicit surface-capturing scheme to determine the wave profile, which is not a trivial task. In comparison, the Lagrangian SPH model is much more advantageous as it can determine the free surface profiles simply by tracing the particle positions. In this field, Zhu et al. (1999) developed a SPH model for the low-Reynolds number incompressible flow inside the porous media and imposed a periodic porous boundary condition on both ends of the computational domain. The porous solid skeleton was discretized and represented by the fixed SPH particles. Tartakovsky and Meakin (2006) applied the SPH method to simulate pore-scale flow transportations and analysed the effects of fluid wetting behaviour and surface tension. Herrera et al. (2009) derived a new SPH formulation for the simulation of advective-dispersive solute transport in an heterogeneous porous media. Using the micro-CT images of rock samples, Ovaysi and Piri (2010) modelled the incompressible viscous flow inside a porous rock by Moving Particle Semi-implicit (MPS) method. Then Ovaysi and Piri (2012) employed the GPU acceleration technology to reduce the computational load of their MPS model. Although the above modelling efforts resolve the flow at the pore scale and can reveal very detailed information of the flow motion, they are extremely computationally expensive even with the use of the GPU, thus not yet practical for the engineering purpose.

The first ISPH model for wave interactions with porous media in the large scale was proposed by Shao (2010). The model solves the spatially-averaged flow field of the porous region without considering the details of the pore flow. The effect of solid skeletons in the porous structure was determined by adding the frictional terms into the momentum equations. Under the same assumption, Akbari and Namin (2013) improved the ISPH approach by introducing a refined background mesh with porosity information to treat the interface boundary. Different particle sizes were also used in the pure fluid zone and porous zone, respectively. Then Akbari (2014) further considered the particle density change within the porous media and validated the improved model via simulating dam-break flow through a porous zone and wave overtopping over a caisson breakwater. More recently, Ren et al. (2014) proposed an improved weakly compressible SPH (WCSPH) model, in which the tangential velocities were averaged near the porous interface so that almost continuous pressure fields can be obtained. Other significant progresses in the ISPH model development can be found in Khayyer et al. (2008), Lind et al. (2012) and Gotoh et al. (2014).

In this study, another simple and straightforward treatment is proposed to deal with the interface boundary between the pure fluid and porous regions, in which an interface zone is specified around the interface line and the particle pressure is averaged within this zone by using the SPH kernel function. In order to verify the proposed boundary treatment, the ISPH model is first applied to the wave damping over a porous bed and the numerical results are compared with the theoretical solutions of Packwood and Peregrine (1980). Then the model is applied to investigate the main features of the flow field, such as velocity and pressure, around and inside a submerged porous breakwater under the action of waves. Comparisons of the wave surface profiles and velocity fields with the experimental data of Wu and Hsiao (2013) are carried out to evaluate the capacity of ISPH model in the porous flow simulations.

2 Governing equations

When considering large-scale porous flows, the governing equations for the flow inside and outside of the porous media are different. del Jesus et al. (2012) analysed the two main sets of governing equations for the porous flow and revealed that there is no universal equation either due to the frictional term or due to the closure model used in the momentum equations. In this work, the unsteady 2D NS equations in the Lagrangian form are used for solving the flow outside of porous media. The NS-type equations, originally proposed by Huang et al. (2003) for porous flow in the Eulerian form, are recast in the Lagrangian form for solving the flow inside porous media.

2.1 Equations for flow outside porous media

Following Huang et al. (2003) and Shao (2010), the flow outside of the porous media is considered as laminar and can be solved by the two-dimensional unsteady Navier-Stokes equations. The Lagrangian form of these equations is expressed as

$$\frac{1}{\rho}\frac{d\rho}{dt} + \nabla \cdot \mathbf{u}_w = 0 \tag{1}$$

$$\frac{d\mathbf{u}_w}{dt} = -\frac{1}{\rho}\nabla P + \mathbf{g} + v\nabla^2 \mathbf{u}_w \tag{2}$$

where ρ = density; t = time; $\mathbf{u}_w$ = flow velocity outside of porous structure; P = pressure; g = gravitational acceleration; and v = laminar viscosity.

It should be mentioned that the turbulence model is not considered in Eq. (2), similar to the approach taken by Huang et al. (2003), in order to simplify the interface boundary conditions. Higuera et al. (2013) commented that the inclusion of turbulence model could greatly improve the breaking wave simulations. Thus the case studies selected in this paper are limited to the non-breaking situations.

2.2 Equations for flow inside porous media

Again by following Huang et al. (2003) and Shao (2010), for the flow inside of the porous media the NS equations with added linear and nonlinear drag force terms are used, which are

$$\frac{1}{\rho}\frac{d\rho}{dt} + \nabla \cdot \mathbf{u}_p = 0 \tag{3}$$

$$\frac{d\mathbf{u}_p}{dt} = -\frac{1}{\rho}\nabla P + \mathbf{g} + v\nabla^2 \mathbf{u}_p - \frac{vn_w}{K_P}\mathbf{u}_p - \frac{C_f n_w^2}{\sqrt{K_P}}\mathbf{u}_p |\mathbf{u}_p| \tag{4}$$

where n_w = porosity of the porous media; K_P = intrinsic permeability; and C_f = nonlinear resistance coefficient. Here $\mathbf{u}_p$ is the discharge velocity, which equals to the seepage velocity multiplied by the porosity of the porous media. Discharge velocity is also referred to as the apparent velocity in various porous flow literatures. Since the particle velocity is used as the apparent velocity in the governing equations, no further velocity treatment is required to satisfy the Beavers and Joseph boundary conditions (Ren et al., 2014). This is a distinct advantage of the particle approach in simulating wave interactions with the porous structures.

The left-hand-side of Eq. (4) is in the form of a full derivative. Comparing Eq. (4) with the counterpart in Huang et al. (2003), it can be seen that if the inertia coefficient equals to unity, the LHS of the momentum equation can be written as a full derivative of the particle velocity. The inertial coefficient denotes the added mass effect for accelerating the fluids in porous media (Liu et al., 1999), whose value is generally known for an isolated simple body but unclear for the random and densely packed materials. Therefore, many researchers, such as Huang et al. (2003, 2008), Akbari and Namin (2013) and Ren et al. (2014) simply neglected the effect of inertia coefficient in their studies.

The last two terms on the RHS of the momentum Eq. (4) represent the effect of fixed porous solid skeleton, with the linear term representing the low Reynolds number flow and nonlinear term representing the high Reynolds number flow, respectively, by following Huang et al. (2003; 2008). Karunarathna and Lin (2006) had also derived various nonlinear frictional forces for the high Reynolds number flows. According to Huang et al. (2003; 2008), if the porosity n_w and stone size d of the porous materials are known, the intrinsic permeability K_P can be determined by the following empirical formula as

$$K_P = 1.643 \times 10^{-7} \left[\frac{d_{50}}{d_0}\right]^{1.57} \frac{n_w^3}{(1-n_w)^2}, \qquad d_0 = 0.01\text{m} \tag{5}$$

and the nonlinear resistance coefficient can be evaluated by using the formula given by

4

$$C_f = 100 \left[d_{50}\left(m\right) \left(\frac{n_w}{K_p}\right)^{1/2} \right]^{-1.5} \tag{6}$$

3   Solution procedure

By using the fractional steps, the Navier-Stokes equations are solved by a prediction–correction procedure in the incompressible SPH approach. The first step -- the prediction step is an explicit integration in the time, based on the laminar and gravitational forces as well as the linear and nonlinear drag forces. So the intermediate particle velocity and position are calculated from the momentum equation without the pressure gradient term as:

$$\Delta \mathbf{u}_* = \left(\mathbf{g} + v\nabla^2 \mathbf{u} - \frac{v n_w}{K_P} \mathbf{u} - \frac{C_f n_w^2}{\sqrt{K_P}} \mathbf{u}\left|\mathbf{u}\right| \right)_t \Delta t \tag{7}$$

$$\mathbf{u}_* = \mathbf{u}_t + \Delta \mathbf{u}_* \tag{8}$$

$$\mathbf{r}_* = \mathbf{r}_t + \mathbf{u}_* \Delta t \tag{9}$$

where $\Delta \mathbf{u}_* =$ changed particle velocity during the prediction step; $\Delta t =$ time increment; $\mathbf{u}_t$ and $\mathbf{r}_t =$ particle velocity and position at time t; and $\mathbf{u}_*$ and $\mathbf{r}_* =$ intermediate particle velocity and position, respectively. The subscript p in $\mathbf{u}_p$ has been dropped for the simplicity.

The pressure is calculated by the classical pressure Poisson equation based on the relative density variance as follows (Shao and Lo, 2003):

$$\nabla \cdot \left(\frac{1}{\rho_*} \nabla P_{t+1} \right) = \frac{\rho_0 - \rho_*}{\rho_0 \Delta t^2} \tag{10}$$

where $\rho_0 =$ initial constant particle density; $\rho_* =$ intermediate particle density after the prediction step; and $P_{t+1} =$ particle pressure at time $t+1$. In our previous studies, it has been found that the above density-invariant source term formulation could cause non-physical particle and pressure noises in some wave applications. However, this method generally performs quite well for the solitary wave condition due to its ordered motion of the fluid particles during the single wave event. For the periodic waves, however, other types of models or more advanced source term treatments should be considered, such as documented by Hu and Adams (2007), Xu et al. (2009) and Khayyer and Gotoh (2011).

Then in the second step -- the correction step, the pressure gradient term is incorporated into the momentum equations to enforce the incompressibility. Once being solved in a fully implicit way, the pressure is used to correct the particle velocity in the following way

$$\Delta \mathbf{u}_{**} = -\frac{1}{\rho_*} \nabla P_{t+1} \Delta t \tag{11}$$

$$\mathbf{u}_{t+1} = \mathbf{u}_* + \Delta \mathbf{u}_{**} \tag{12}$$

where $\Delta\mathbf{u}_{**} =$ changed particle velocity during the correction step. Finally, the new particle positions are time-centred by following Eq. (13)

$$\mathbf{r}_{t+1} = \mathbf{r}_t + \frac{\mathbf{u}_{t+1} + \mathbf{u}_t}{2}\Delta t \tag{13}$$

where $\mathbf{u}_{t+1}$ and $\mathbf{r}_{t+1} =$ particle velocity and position at time $t+1$, respectively. As mentioned by Akbari and Namin (2013) and Ren et al. (2014), the solved particle velocity from the porous flow equations is the apparent velocity, which is equal to the particle velocity of the pure fluid flow. Therefore, the proposed momentum Eqs. (2) and (4) can be solved simultaneously in the entire domain by setting the frictional terms to be zero for the fluid zone.

4   SPH methodology

4.1   SPH formulas

The key feature of the SPH is that it is an interpolation method, which allows the physical quantity and any function of interest to be obtained by summation of relevant physical quantities and functions (Monaghan, 1992). The summation usually can be expressed in terms of the values at a set of disordered points within the range of the support domain. The value of any field function $A(\mathbf{r})$ at point $\mathbf{r}$ can be expressed as

$$A(\mathbf{r}) = \int A(\mathbf{r}')W(\mathbf{r} - \mathbf{r}', h)d\mathbf{r}' \tag{14}$$

where $W(\mathbf{r} - \mathbf{r}', h)$ is the interpolating kernel function; and h is the smoothing length. In SPH numerical simulations, the integral interpolant is calculated by a summation interpolant in the discrete notation as

$$A_a(\mathbf{r}) = \sum_b m_b \frac{A_b(\mathbf{r})}{\rho_b}W_{ab} \tag{15}$$

where a and b denote the reference particle and its neighbour; W_{ab} is the kernel function value between the two particles; and m_b and ρ_b are the mass and density of neighbouring particle b, respectively. As a result, the density of particle a is expressed as

$$\rho_a = \sum_b m_b W_{ab} \tag{16}$$

In order to ensure the linear and angular momentum conservation, the following asymmetric pressure gradient term is used in this study

$$\left(\frac{1}{\rho}\nabla P\right)_a = \sum_b m_b\left(\frac{P_a}{\rho_a^{\,2}} + \frac{P_b}{\rho_b^{\,2}}\right)\nabla_a W_{ab} \tag{17}$$

where $\nabla_a W_{ab}$ is the gradient of the kernel function taken with respect to the position of particle a. Similarly the divergence of vector $\mathbf{u}$ at a given particle a can also be estimated by

$$\nabla \cdot \mathbf{u}_a = \rho_a \sum_b m_b \left(\frac{\mathbf{u}_a}{\rho_a^2} + \frac{\mathbf{u}_b}{\rho_b^2} \right) \cdot \nabla_a W_{ab} \tag{18}$$

The viscous force terms in Eqs. 2 and 4 can be formulated by combining the above gradient and divergence operators as

$$(\nu_0 \nabla^2 \mathbf{u})_a = \sum_b m_b \frac{2(\nu_a + \nu_b)}{\rho_a + \rho_b} \frac{\mathbf{u}_{ab} \mathbf{r}_{ab} \cdot \nabla_a W_{ab}}{|\mathbf{r}_{ab}|^2 + \eta^2} \tag{19}$$

where η is a small number to keep the denominator non-zero and commonly set to $0.1h$.

Due to the high sensitivity of pressure to the particle disorders, the Laplacian in the pressure Poisson equation is formulated through a hybrid of the standard SPH first-order derivative plus a first-order finite difference scheme as (Shao and Lo, 2003)

$$\nabla \cdot \left(\frac{1}{\rho} \nabla P \right)_a = \sum_b m_b \frac{8}{(\rho_a + \rho_b)^2} \frac{P_{ab} \mathbf{r}_{ab} \cdot \nabla_a W_{ab}}{|\mathbf{r}_{ab}|^2 + \eta^2} \tag{20}$$

where $P_{ab} = P_a - P_b$ and $\mathbf{r}_{ab} = \mathbf{r}_a - \mathbf{r}_b$.

4.2   Kernel function

The cubic spline kernel function developed by Monaghan (1992) has been used to solve many kinds of hydrodynamic problems, and it has the following form

$$W(r,h) = \begin{cases} \dfrac{10}{7\pi h^2} \left(1 - \dfrac{3}{2}q^2 + \dfrac{3}{4}q^3 \right) & 0 \le q < 1 \\ \dfrac{10}{28\pi h^2}(2-q)^3 & 1 \le q \le 2 \\ 0 & q > 2 \end{cases} \tag{21}$$

where $r = $ separation distance between the reference particle and neighbouring particle; and $q = \dfrac{r}{h}$ is the relative distance. The radius of the kernel influence is set to be twice of the smoothing length. Here it should be noted that nowadays the so-called Wendland kernel (1995) has been found to offer much more satisfactory performance in some SPH applications.

5 Boundary conditions

5.1 Free surface boundary

As for the free surface particles, the number of their neighbouring particles is significantly less than that of the inner fluid particles, since no particle exists in the outer region of the free surface. So the free surface particles can be easily identified by the particle density that drops sharply (Shao and Lo, 2003) due to the truncated support zone of the kernel. According to common computational experience, if the density drop of a particle is below 1% ~ 10% of the reference value, it can be regarded as a surface particle. A zero pressure shall be applied to the surface particles as known conditions in the PPE solution.

5.2 Solid boundary

Solid walls are represented by the fixed wall particles with the same particle distance as the inner fluid particles. The wall particles balance the pressure of the inner fluid particles and keep them at appropriate distance from the solid wall, neither penetrating nor going far away. The velocity boundary conditions are set as the non-slip boundaries in all of the following studies. Since the kernel compact support zone is truncated for a particle near the wall, the dummy particles are added to implement the Dirichlet boundary for the velocity and Neumann boundary for the pressure. Several lines of the dummy particles are used in order to keep the fluid density near the wall consistent with that of the inner fluids. The wall particles are also included in the pressure solution process, during which the Neumann boundary conditions are imposed on the wall and dummy particles.

5.3 Wave maker boundary

In our study, the solitary waves will be used to verify and validate the proposed model, because the solitary wave is frequently considered to have certain characteristics of tsunamis, storm surges and other long period waves, which are of great importance in the coastal engineering. The mathematical solution of a solitary wave is a function of distance x and time t, derived from the Boussinesq equations (Lee et al., 1982) as below

$$\eta(x,t) = A \sec h^2 \left[\sqrt{\frac{3A}{4d^3}} (x - ct) \right] \tag{22}$$

where η = water surface elevation; A = wave amplitude or wave height; d = water depth; and the speed of wave c is given by

$$c = \sqrt{g(d + A)} \tag{23}$$

To generate the numerical solitary wave, a solid wave paddle is put on one side of the water flume and the displacement of the wave paddle follows (Lee et al., 1982)

$$X_P(t) = \frac{A}{kd} \tanh\left(k(X_P(t) - ct)\right) \tag{24}$$

where $k = \sqrt{\frac{3A}{4d^3}}$.

5.4   Wave absorbing boundary

By adopting a long enough distance on the downstream side of the numerical water tank, the wave reflection from concerned areas can be reduced. Sometimes this is not practical, as when the simulation domain is large, a large number of particles would be required to achieve the computational accuracy at heavy CPU cost. Some effective ways have been proposed to solve the problem of wave reflections. For instance, Xu (2010) and Li et al. (2012) set up a damping zone to absorb the wave reflection in a way widely used in the Boussinesq models and they demonstrated that this method is also quite effective in the SPH modelling.

In the present paper the similar damping zone approach is used. In the damping zone, the fluid particle velocity is a function of the distance from the end side of the water tank, and the damping process is achieved by using

$$U_d = U_0 f(x) \tag{25}$$

where U_d is the dampened velocity; and U_0 is the particle velocity at the start line ($x = x_0$) of the damping zone. As for the damping function, it has the following form as

$$f(x) = 1 - e^{\left(-\beta\left(L_d - (x - x_0)\right)\right)} \tag{26}$$

According to Xu (2010) and Li et al. (2012), a value of 2.0 can be used for β. L_d is the total length of the damping zone that is related to the simulated wave length.

5.5   Interface boundary

The most difficult issue to treat in a porous flow is the flow exchange across the interface boundary between the pure fluid flow and porous flow regions. Since SPH is a Lagrangian particle method, the flow exchange means that the fluid particles near the interface should be allowed to move across the porous interface and relocate in different flow media regions freely at each computational time step. The physical boundary conditions at the interface are the continuity of the velocities and continuity of the normal and tangential stresses (Beavers and Joseph, 1967), expressed as

$$\mathbf{u}_w = n_w \mathbf{u}_p \tag{27}$$

$$\left(n_i \sigma_{ij} n_j\right)_w = \left(n_i \sigma_{ij} n_j\right)_p \tag{28}$$

$$\left(\tau_i \sigma_{ij} n_j\right)_w = \left(\tau_i \sigma_{ij} n_j\right)_p \tag{29}$$

where the subscript w denotes the physical variable in the water region, while p denotes that in the porous region; σ_{ij} are the stress tensors; and τ_i and n_i denote the tangential and normal unit vector to the interface, respectively.

These interface boundary conditions have been simplified into a two-dimensional form by Huang et al. (2003) in simulating a solitary wave propagation over a submerged porous breakwater. In order to implement such similar boundary conditions in ISPH, an imaginary grid line was used by Shao (2010) at the interface between the two flow regions. The computation of each flow region was carried out separately. Unfortunately this method is complicated to use and also not entirely consistent with the Lagrangian nature of the SPH, as pointed out by Akbari and Namin (2013). By assuming that the porous interface is not a sharp line but encompassing a transitional zone, Akbari and Namin (2013) proposed a novel

boundary treatment method by introducing a finer background mesh with porosity information for both the porous and pure fluid regions. This method allows more detailed porosity information to be obtained for the computations near the interface. By adopting similar idea, in the present work a more straightforward but equally effective interface treatment method is proposed for the ISPH applications in the wave interaction with porous structures. Instead of only using a single interface line, an interface zone is placed between the two flow regions with the interface line being located at the centre of the zone, as shown in Fig. 1. Therefore, two areas are separated on both sides of the interface boundary line, the fluid part and the porous part each with a width $2D_0$, where D_0 is the distance between the particles.

By using the proposed ISPH interface model, at each computational time step the fluid pressures of the particles within the interface zone are averaged by the SPH kernel function after solving the pressure Poisson equation. Only the neighbouring particles located within the interface zone are included in the summations. Meanwhile, the interface boundary conditions can automatically meet the continuities of the normal and tangential stresses due to the particle velocity being the apparent velocity in the governing equations (Ren et al., 2014). Then the velocity and position of interface zone particles are updated by using this revised pressure field, which has already included the influence of flow exchanges at the interface. With this treatment, more continuous velocity and pressure fields are achieved in the vicinity of the interface between the outside and porous flows. This approach could be considered to be better than the interface boundary treatment proposed by Ren et al. (2014), since the tangential velocity across the porous interface is generally not continuous, thus it should be physically unrealistic to average out these velocity differences.

6 Case I: Solitary wave attenuation over a porous bed

6.1 Description of model setup

The accuracy of the improved ISPH flow model for porous structures is firstly verified by comparing the numerical results of solitary wave damping over a porous bed with the theoretical solutions of Packwood and Peregrine (1980). After the model is verified, it will be used to investigate the main features of flow field around and inside a submerged porous breakwater in the next section. A schematic diagram of the model setup is shown in Fig. 2. The computational zone includes both the water region and the porous region. A solitary wave is generated on the left side of the numerical flume with the initial wave height H_i. The still water depth is h_0, and the depth of the porous bed is h_p with porosity n_w. As shown in Fig. 2, the intersection of the left boundary and the flume bottom is defined as (x, z) = (0, 0). The wave tank is 46.0 m long and 0.52 m high. The starting point of the porous bed is $X_s = 3.0$ m away from the coordinate origin of the computational domain. S_0 is the stroke of the wave paddle.

6.2 Comparisons of wave height attenuation

Packwood and Peregrine (1980) gave the theoretical wave height damping function for solitary wave propagating over a porous bed with finite depth as

$$H = \frac{H_i}{1 + C_s\left(H_i/h_0\right)\left(x/h_0\right)} \tag{30}$$

where x is the distance travelled by the solitary wave; and

$$C_s = 0.4\left(K_h/C_0\right)\left(h_p/h_0\right) \tag{31}$$

$$C_0 = \sqrt{gh_0}\left(1 + H_i/2h_0\right) \tag{32}$$

where K_h represents the hydraulic conductivity of the porous media and can be expressed as

$$K_h = K_p g / \upsilon \tag{33}$$

where $\upsilon =$ kinematic viscosity of the fluid.

The computational parameters used are: water depth $h_0 = 0.4$ m, ratio of depth of porous bed to still water $h_p / h_0 = 1.0$, porosity of bed $n_w = 0.39$ and incident solitary wave height $H_i = 0.11$ m. The mean diameter of porous materials is $d_{50} = 0.55$ cm so the intrinsic permeability coefficient is $K_p = 0.102 \times 10^{-7}$ m^2 according to Eq. (5), and the nonlinear resistance force coefficient is $C_f = 0.51$ as per Eq. (6). The particle spacing is $D_0 = 0.04$ m and about 24 K particles are used in the simulation.

Fig. 3 compares the wave height ratios obtained from the ISPH computations and theoretical solutions of Packwood and Peregrine (1980). The green line with circles represents the theoretical wave attenuation ratios with the increase of the travel distance, while the red line with upper triangular denotes the ISPH results by using the proposed interface boundary treatment and the blue line with diamonds denotes the ISPH results without using the interface treatment. It can be seen that even with this small degree of permeability $K_p = 0.102 \times 10^{-7}$ m^2, the wave height ratio H/H_i could decrease to 0.745 after travelling a distance of 28 m. It can also be seen that, compared with the theoretical solutions, the ISPH computations with the interface boundary treatment have shown much better agreement. As for the discrepancy between the numerical and theoretical results, it could be caused by the numerical errors in the free surface detection with some particles splashing out. The reason for the numerical results being generally lower than the theoretical ones is most likely due to the energy dissipations caused by the friction over bed, as explained by Huang et al. (2008).

6.3 Pressure continuity at the interface

In order to further test the interface boundary treatment, the pressure continuities at the interface are checked by comparing the pressures at the same point of the interface but calculated from different sides of the flow zone. Table 1 presents the coordinates of six pressure measurement points that are in three pairs, i.e. P1 and P2, P3 and P4, P5 and P6. Each pair of the points has the same x coordinate but a very tiny difference in the z coordinate, so that they can be considered to be at the same position. z = 0.001 m means that the location is in the pure water area, while z = -0.001 m means that the location is in the porous area. For illustration, these measurement points are also shown in Fig. 2.

Fig. 4 shows the time histories of dynamic pressure at these six measurement points. As can be seen from the pressure curves, each pair of the pressure points matches its counterpart

(i.e. P1 to P2, P3 to P4, P5 to P6) quite well throughout the simulation time, including all the peak values as well as the pressure fluctuations. This has demonstrated the effectiveness of the proposed interface boundary treatment to achieve good pressure continuities.

7   Case II: Solitary wave interaction with a submerged porous breakwater

7.1   Description of numerical modelling

A numerical simulation was carried out using the proposed ISPH model to reproduce the experiment of Wu and Hsiao (2013). The physical experiment was conducted in a 2D narrow wave flume that was 25 m long, 0.5 m wide and 0.6 m high. The left hand side of the flume was equipped with a piston-type wave-maker to generate the solitary wave and a gravel beach was installed on the right side of the flume to dissipate wave energy and reduce wave reflection (Wu and Hsiao, 2013). The flume bottom was a solid boundary and the right side of the computational domain was an absorbing boundary. A permeable cuboid structure was mounted on the bottom in the middle of the wave flume, which was composed of uniform-sized spheres with a constant diameter d_{50} = 1.5 cm and 13 cm long, 6.5 cm high and 50 cm wide with a porosity of 0.52. As shown in Fig. 5 for the computational model, the time histories of free surface elevation were obtained by two wave gauges located in front of (x = −1.8 m, WG1) and behind (x = +1.8 m, WG2) the porous breakwater. The velocity field was measured by a particle image velocimetry (PIV) in the vicinity of the permeable breakwater in the experiment, which is also used here for validating the numerical model. The constant water depth was 0.106 m, with the wave height to water depth ratio of 0.45. More details about the experiment can be found in Wu and Hsiao (2013).

As the porous breakwater in the experiment fully occupied the wave flume in the lateral direction, this can be regarded as a 2D problem in the macroscopic scale. As shown in Fig. 5, the intersection of the weather side of the porous breakwater and flume bottom is defined as (x, z) = (0, 0). The numerical wave tank is 8.0 m long and 0.2 m high, with a porous region in the middle of the wave tank, which is shorter than the experimental flume. The weather side of the breakwater is 4.0 m away from the left side of the computation domain. Since the length of the computational domain is shorter than the experimental wave flume (25 m) due to the CPU constrains, instead of imposing the experimental wave height, the numerical incident wave height 0.477 m was determined by matching the numerical wave height at reference wave gauge WG_1 with the experimentally-measured one through the trials-and-errors. The downstream boundary was a wave absorbing boundary to prevent wave reflections. The bottom of the wave tank was treated as non-slip velocity boundary. The particle spacing is 0.005 m, with about 36 K particles in the simulation. The particle spacing in the porous region is the same as that in the fluid area. This setup can ensure both computational efficiency and accuracy as only about 3.5 hours were needed for 8 s simulations by using a computer of CPU 3.33 GHz.

7.2   Comparisons between model results and experimental data

Fig. 6 shows the comparison of time series of free surface elevation between present ISPH model results and experimental data of Wu and Hsiao (2013). As can be seen the wave curve at reference point x = -1.8 m fits fairly well with the experimental measurement, especially for the incident wave as shown in Fig. 6 (a). This means the numerically-generated incident wave is a close representation of the laboratory wave. The incident wave is partially

reflected by the submerged porous breakwater after 4 s. The reflected wave propagates in the opposite direction towards the wave gauge point x = -1.8m, resulting in a waveform similar to the sine wave shape. There exist some kinds of free surface fluctuations, which could be attributed to our extraction of the free surface by averaging three particles in the neighbourhood. Averaging more particles could lead to much smoother results but may comprise the numerical accuracy in capturing the peak values. Likewise, Fig. 6 (b) shows the numerical predictions of wave time series at x = 1.8 m, which also match well with the experimental measurements. It is noted that there is a slight overestimation of the wave surface at the wave trough in the numerical results and this may be due to the friction caused by the porous structure on the flow being slightly underestimated by the model.

Fig. 7 (a) ~ (e) shows the comparisons of flow velocity field between model results (right) and experiment (left) at five different instantaneous time t = 1.45 s, 1.65 s, 1.85 s, 2.05 s and 2.25 s, respectively. These representative times were chosen to show the flow features around and inside the submerged porous breakwater at five wave evolution phases of interest, from wave approaching the porous breakwater until leaving it. The different colours in each velocity vector field represent the instantaneous pressures.

As it can be seen from Fig. 7 (a), the free surface elevations, as well as the flow patterns, are accurately predicted by the model. When the leading wave front approaches the weather side of the porous breakwater at t = 1.45 s, the particle velocity directions are changed due to the impediment of the breakwater, resulting in the flow separation at the top of the obstacle and generation of a small vortex on the upper left face of the structure. Although the velocity is small, the flow is seen to penetrate the porous breakwater and flows from the lee side to the pure fluid zone. Despite the general agreement, slightly disturbed velocities can be observed on the lee side of the obstacle in the experimental measurement as shown in the left image of Fig. 7 (a). This is because the breakwater is composed of regularly-spaced spheres with uniform size in the experiment and therefore the flow can only pass through the gaps among the spheres with no flow flux on the sphere face. However, in the ISPH model the porous region was treated as being spatially-averaged and macroscopically-homogeneous and thus the fluid particles could penetrate the lee face of the breakwater at every point.

As shown in Fig. 7 (b) (t = 1.65 s) and (c) (t = 1.85 s), with the increase in time, a large vortex is generated on the lee side of the breakwater, which is strengthened by the shear layers due to the flow convection and wave-structure interactions. After that, it starts to move upward to the free surface as shown in Fig. 7 (d) (t = 2.05 s), causing it to bulge slightly near the free surface in the experiment. When the wave has completely passed by the breakwater, the main vortex nearly reaches the free surface as shown in Fig. 7 (e) (t = 2.25 s), and the velocity disturbance occurs beneath the surface just above the vortex. Generally speaking, the ISPH model has simulated fairly well the locations of the centroid of the vortex as well as its dimension and entire evolution process. The noise-free pressure fields demonstrate the stable numerical simulations even across the interface boundary. However, it should also be realized that the distribution of some of the free-surface particles still does not seem to be physically realistic. This could be partly attributed to the inadequate spatial resolutions and the lack of turbulence modelling.

Fig. 8 (a) ~ (e) shows the velocity profiles at seven different sections in the x direction. Table 2 presents the coordinates of these velocity measurement points. It should be noted that the coordinates of point V6 and V7 are different at t = 1.45 s and other times (t = 1.65, 1.85, 2.05 and 2.25 s). In all the figures, the circle denotes the experimental velocity, and the red solid line denotes the horizontal velocity distribution and the green one denotes the vertical velocity distribution along the z direction, respectively, for the ISPH results.

The measured and modelled results are generally in good agreement, as shown in Fig. 8 (a) ~ (e), especially for the vertical velocity distributions, thus justifying the 2D numerical

modelling approach. The differences between the numerical and experimental horizontal velocity distributions most happen around the circulation zone at x = 0.16 m after the solitary wave passes over the porous breakwater. The interface boundary treatment is seen to perform quite well as fairly good match at all of the measuring sections near the porous structure has been achieved. For the comparison of horizontal velocity profiles, the numerical predictions for the location around the main vortex, i.e., x = 0.16 m, showed unsatisfactory agreement with the measurement, as shown in Fig. 8 (b) ~ (e). The ISPH results show a mostly uniform profile whereas the measured results are distorted due to the presence of vortex despite the fact some previous studies compared with the same dataset have showed quite satisfactory agreement on the velocity and even the turbulence properties (Ma et al., 2014; Wu and Hsiao, 2013; Wu et al., 2014). The reasons could be attributed to the over-simplified way of drag force being added into the momentum equations or could be due to the deficiencies in the interface boundary treatment. Further refining the spatial resolution of the model could help improve the model performance but can only be achieved at heavy CPU expenses.

As the leading wave front of the solitary wave approaches the weather side of the breakwater, the experimental results show a small horizontal velocity perturbation on the lee side of the obstacle at x = 0.14 m, whereas the ISPH results show a uniform velocity profile, as shown in Fig. 8 (a). This feature is consistent with the velocity field shown in Fig. 7 (a), with the reasons being explained before. So we can realize that the flow was affected by the local geometry of the breakwater and the flow features could largely depend on the x coordinate of the measurement sections. The velocity differences as shown in Fig. 8 (a) occur in the initial stage of the formation of the primary vortex. As the solitary wave further propagates towards the lee edge of the obstacle, this velocity difference between the measured and calculated results also shifts to the location x = 0.16 m as shown in Fig. 8 (b). Besides, they appear in both the horizontal and vertical velocity profiles at this location. With the increase of time from t = 1.85 s to 2.25 s, the horizontal velocity differences continue to exist, whereas the vertical velocity differences gradually reduce until a satisfactory agreement with the experimental data is obtained. This is demonstrated at both x = 0.16 m and 0.20 m in Fig. 8 (c) ~ (e). This indicates that the model can well predict the vertical velocity profiles for most of the measuring sections. As the interface boundary between the porous and outside flow regions is located at z = 0.065 m and x = 0.0 m and 0.13 m in the computational domain, the velocity profiles in Fig. 8 demonstrated that the proposed ISPH interface flow model can satisfactorily reproduce the flow velocity changes near the important areas of the interface.

7.3   Sensitivity study of model convergence and interface boundary treatment

To check the convergence of the ISPH porous flow model, two additional computations have been made with a coarser and finer particle spacing of 0.0065 m and 0.0035 m, as compared with the original run using particle spacing of 0.005 m. The computed horizontal and vertical velocity distributions along the depth on both sides of the porous breakwater, are shown in Fig. 9 (a) and (b), respectively, for the location of x = -0.04 m and 0.08 m at selected time t = 2.05 s. The comparisons showed very little differences among the three numerical runs indicating the convergence of the model results. We can also find out that the most refined computations using particle size 3.5 mm seem to agree best with the experimental data of Wu and Hsiao (2013). Nonetheless, it has been found that the convergence property of the model is not as good as expected for the vertical velocity above the porous breakwater as shown in Fig. 9 (b). This is most likely due to our use of the low-order solitary wave theory to generate the numerical waves, which caused more discrepancies in the velocity profile.

To further demonstrate the improvement of the interface boundary treatment as described in Section 5.5, we have also made another control run to compare the numerical results obtained with and without the proposed interface model. Fig. 10 shows the horizontal and vertical velocity distributions at x = 0.0 m at time t = 1.45 s, when the solitary wave crest is approaching the weather side of the breakwater. In the figure, the circles represent the experimental data of Wu and Hsiao (2013), and the solid and dotted lines represent the ISPH numerical results computed with and without the use of the interface model. It is obvious that the improved model provides more accurate predictions of the velocity profiles especially for the vertical velocity, for which a sharper velocity gradient has been captured near the location of the interface between the outside and porous flow regions.

8   Conclusion

An incompressible SPH model has been developed for investigating the wave interactions with porous structure to explore the flow motions inside and around the structure. An improved interface boundary treatment has been proposed between the porous and outside mean flows by interpolating and averaging the computed particle pressures within the interface boundary zone using SPH kernel functions.

The improved model was first verified by comparing the numerical wave damping ratio against the theoretical solution for the case of solitary wave propagation over a porous bed. As a way of checking the continuity of interface flow variables, the time histories of computed dynamic pressures were compared at three pairs of the measurement point located on both sides of the interface that is close to each other. As a practical application and further evaluation of the model, very detailed investigations have been conducted to explore the flow motions induced by a solitary wave passing through a submerged porous breakwater. The time histories of the free surface and horizontal and vertical velocity profiles at a number of the measuring sections were compared between the ISPH numerical simulations and the experimental data. Again a good agreement is obtained for all of the wave parameters of interest. Although some kinds of discrepancy were found in the flow circulation zone on the lee side of the breakwater, the satisfactory agreement near the interface boundaries provided a strong indication that the improved interface treatment model is more effective to solve the problems of wave interaction with porous structures. Furthermore, model convergence has been checked by using three different particle sizes and almost identical numerical results have been obtained while the most refined computations agreed best with the measured data. Another two control runs have also been carried out by using the ISPH model with and without the improved interface boundary treatment. The computed wave damping height and two velocity distributions along the depth clearly demonstrated that the proposed interface model significantly improved the modelling accuracy and obtained better agreements with the experimental data. We would expect that the inclusion of turbulence model (e.g. Gotoh et al., 2001) and further refinement of the particle spatial resolutions could better improve the performance of the model.

Acknowledgements

References

Akbari, H., 2014. Modified moving particle method for modeling wave interaction with multi layered porous structures. Coastal Engineering 89, 1-19.

Akbari, H., Namin, M.M., 2013. Moving particle method for modeling wave interaction with porous structures. Coastal Engineering 74, 59-73.

Beavers, G.S., Joseph, D.D., 1967. Boundary conditions at a naturally permeable wall. Journal of Fluid Mechanics 30(1), 197-207.

del Jesus, M., Lara, J.L., Losada, I.J., 2012. Three-dimensional interaction of waves and porous coastal structures: Part I: Numerical model formulation. Coastal Engineering 64, 57-72.

Garcia, N., Lara, J.L., Losada, I.J., 2004. 2-D numerical analysis of near-field flow at low-crested permeable breakwaters. Coastal Engineering 51(10), 991-1020.

Gotoh, H., Khayyer, A., Ikari, H., Arikawa, T., Shimosako, K., 2014. On enhancement of Incompressible SPH method for simulation of violent sloshing flows. Applied Ocean Research 46, 104-115.

Gotoh, H., Shibahara, T., Sakai, T., 2001. Sub-particle-scale turbulence model for the MPS method—Lagrangian flow model for hydraulic engineering, Computational Fluid Dynamics Jour. 9(4):339–347.

Herrera, P.A., Massabó, M., Beckie, R.D., 2009. A meshless method to simulate solute transport in heterogeneous porous media. Advances in Water Resources 32(3), 413-429.

Higuera, P., Lara, J.L., Losada, I.J., 2013. Simulating coastal engineering processes with OpenFOAM®. Coastal Engineering 71, 119-134.

Hu, K.-C., Hsiao, S.-C., Hwung, H.-H., Wu, T.-R., 2012. Three-dimensional numerical modeling of the interaction of dam-break waves and porous media. Advances in Water Resources 47, 14-30.

Hu, X.Y., Adams, N.A., 2007. An incompressible multi-phase SPH method. Journal of Computational Physics 227(1), 264-278.

Hsu, T.-J., Sakakiyama, T., Liu, P.L.F., 2002. A numerical model for wave motions and turbulence flows in front of a composite breakwater. Coastal Engineering 46(1), 25-50.

Huang, C.-J., Chang, H.-H., Hwung, H.-H., 2003. Structural permeability effects on the interaction of a solitary wave and a submerged breakwater. Coastal Engineering 49(1–2), 1-24.

Huang, C.J., Shen, M.L., Chang, H.H., 2008. Propagation of a solitary wave over rigid porous beds. Ocean Engineering 35(11-12), 1194-1202.

Karunarathna, S.A.S.A., Lin, P., 2006. Numerical simulation of wave damping over porous seabeds. Coastal Engineering 53(10), 845-855.

Khayyer, A., Gotoh, H., 2011. Enhancement of stability and accuracy of the moving particle semi-implicit method. Journal of Computational Physics 230(8), 3093-3118.

Khayyer, A., Gotoh, H., Shao, S.D., 2008. Corrected incompressible SPH method for accurate water-surface tracking in breaking waves. Coastal Engineering 55 (3), 236-250.

Kobayashi, N., Wurjanto, A., 1990. Numerical model for waves on rough permeable slopes. Journal of Coastal Research, 149-166.

Lara, J.L., Garcia, N., Losada, I.J., 2006. RANS modelling applied to random wave interaction with submerged permeable structures. Coastal Engineering 53(5–6), 395-417.

Lee, J.-J., Skjelbreia, J.E., Raichlen, F., 1982. Measurmment of velocities in solitary waves. Journal of Waterway, Port, Coastal, and Ocean Division 108(2), 200-218.

Li, J., Liu, H., Gong, K., Tan, S.K., Shao, S., 2012. SPH modeling of solitary wave fissions over uneven bottoms. Coastal Engineering 60, 261-275.

Lind, S.J., Xu, R., Stansby, P.K., Rogers, B.D., 2012. Incompressible smoothed particle hydrodynamics for free-surface flows: A generalised diffusion-based algorithm for stability and validations for impulsive flows and propagating waves. Journal of Computational Physics 231 (4), 1499-1523.

Liu, P.L.F., Lin, P., Chang, K.A., Sakakiyama, T., 1999. Numerical modeling of wave interaction with porous structures. Journal of Waterway, Port, Coastal and Ocean Engineering 125(6), 322-330.

Ma, G., Shi, F., Hsiao, S.-C., Wu, Y.-T., 2014. Non-hydrostatic modeling of wave interactions with porous structures. Coastal Engineering 91, 84-98.

Monaghan, J.J., 1992. Smoothed Particle Hydrodynamics. Annual Review of Astronomy and Astrophysics 30(1), 543-574.

Ovaysi, S., Piri, M., 2010. Direct pore-level modeling of incompressible fluid flow in porous media. Journal of Computational Physics 229(19), 7456-7476.

Ovaysi, S., Piri, M., 2012. Multi-GPU acceleration of direct pore-scale modeling of fluid flow in natural porous media. Computer Physics Communications 183(9), 1890-1898.

Packwood, A.R., Peregrine, D.H., 1980. The propagation of solitary waves and bores over a porous bed. Coastal Engineering 3, 221-242.

Ren, B., Wen, H., Dong, P., Wang, Y., 2014. Numerical simulation of wave interaction with porous structures using an improved smoothed particle hydrodynamic method. Coastal Engineering 88, 88-100.

Rojanakamthorn, S., Isobe, M., Watanabe, A., 1989. A mathematical model of wave transformation over a submerged breakwater. Coastal Engineering Japan 32(2), 209-234.

Shao, S., 2010. Incompressible SPH flow model for wave interactions with porous media. Coastal Engineering 57(3), 304-316.

Shao, S., Lo, E.Y.M., 2003. Incompressible SPH method for simulating Newtonian and non-Newtonian flows with a free surface. Advances in Water Resources 26(7), 787-800.

Sollitt, C.K., Cross, R.H., 1972. Wave transmission through permeable breakwaters. Proceedings of 13th International Conference on Coastal Engineering, ASCE, 1827-1846.

Sulisz, W., 1985. Wave reflection and transmission at permeable breakwaters of arbitrary cross-section. Coastal Engineering 9(4), 371-386.

Tartakovsky, A.M., Meakin, P., 2006. Pore scale modeling of immiscible and miscible fluid flows using smoothed particle hydrodynamics. Advances in Water Resources 29(10), 1464-1478.

van Gent, M.R.A., 1995. Wave Interaction with Permeable Coastal Structures. PhD Thesis, Delft University Press, The Netherland.

Wendland, H., 1995. Piecewise polynomial, positive definite and compactly supported radial functions of minimal degree. Advances in Computational Mathematics 4(1), 389-396.

Wu, Y.-T., Hsiao, S.-C., 2013. Propagation of solitary waves over a submerged permeable breakwater. Coastal Engineering 81, 1-18.

Wu, Y.-T., Yeh, C.-L., Hsiao, S.-C., 2014. Three-dimensional numerical simulation on the interaction of solitary waves and porous breakwaters. Coastal Engineering 85, 12-29.

Wurjanto, A., Kobayashi, N., 1993. Irregular wave reflection and runup on permeable slopes. Journal of Waterway, Port, Coastal, and Ocean Engineering 119 (5), 537-557.

Xu, R., 2010. An Improved Incompressible Smoothed Particle Hydrodynamics Method and Its Application in Free-surface Simulations. PhD Thesis, University of Manchester, The United Kindom.

Xu, R., Stansby, P., Laurence, D., 2009. Accuracy and stability in incompressible SPH (ISPH) based on the projection method and a new approach. Journal of Computational Physics 228(18), 6703-6725.

Yu, X., Chwang, A., 1994. Wave motion through porous structures. Journal of Engineering Mechanics 120 (5), 989-1008.

Zhu, Y., Fox, P.J., Morris, J.P., 1999. A pore-scale numerical model for flow through porous media. International Journal for Numerical and Analytical Methods in Geomechanics 23(9), 881-904.

Table 1. The coordinates of pressure measurement points

Measurement points	P1	P2	P3	P4	P5	P6
x (m)	10		15		20	
z (m)	0.001	-0.001	0.001	-0.001	0.001	-0.001

Table 2. The coordinates of velocity measurement points

Measurement points		V1	V2	V3	V4	V5	V6	V7
x (m)	t = 1.45 s	-0.04	0.00	0.04	0.08	0.12	0.14	0.16
	t = other	-0.04	0.00	0.04	0.08	0.12	0.16	0.20
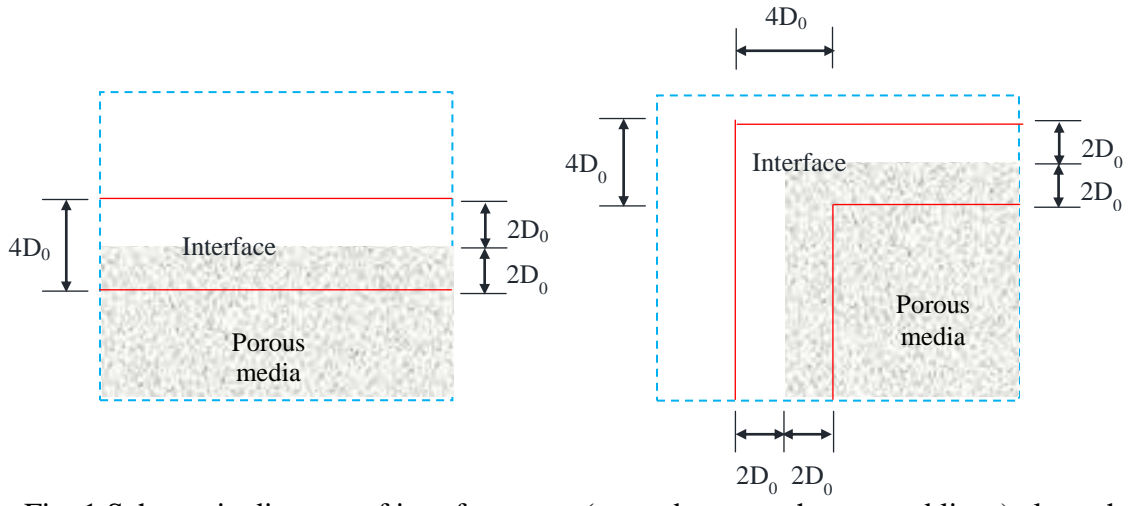
Fig. 1 Schematic diagram of interface zone (space between the two red lines) along the interface boundary line
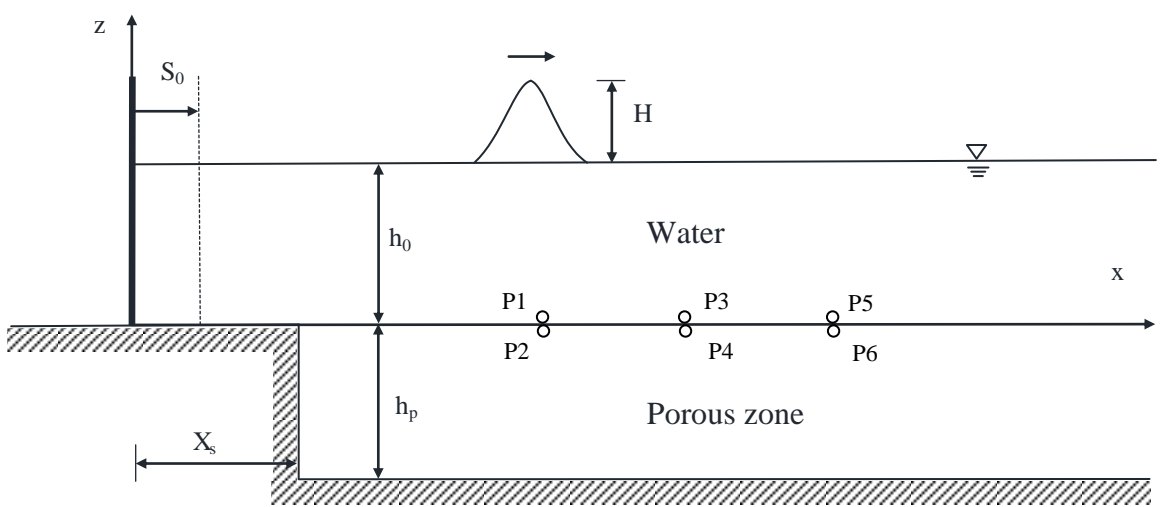
Fig. 2 Schematic diagram of solitary wave propagating over a porous bed
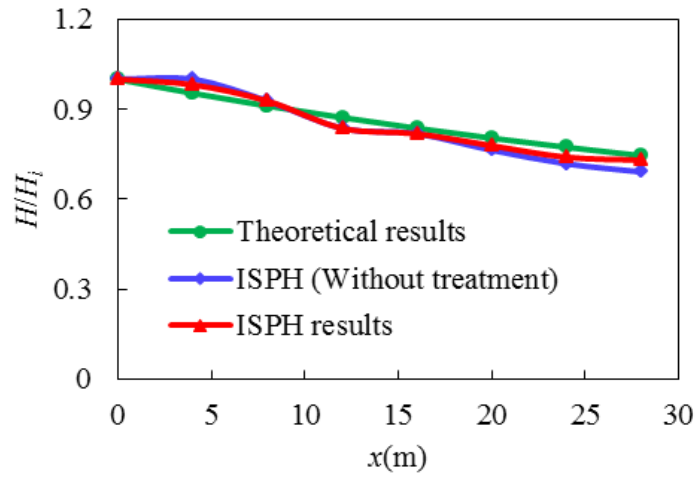
Fig. 3 Comparisons of ISPH and theoretical wave attenuation heights for solitary wave propagating over a porous bed
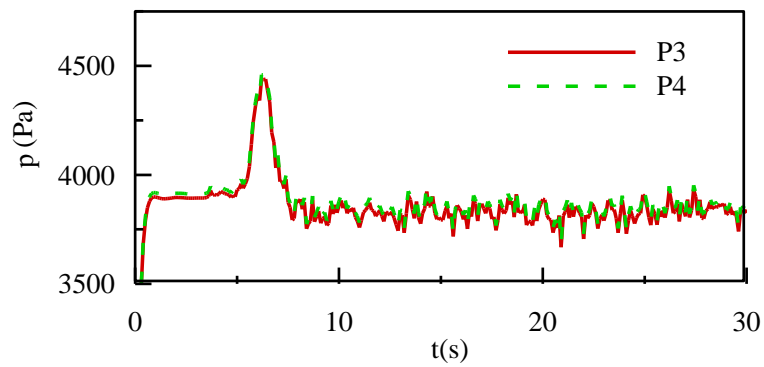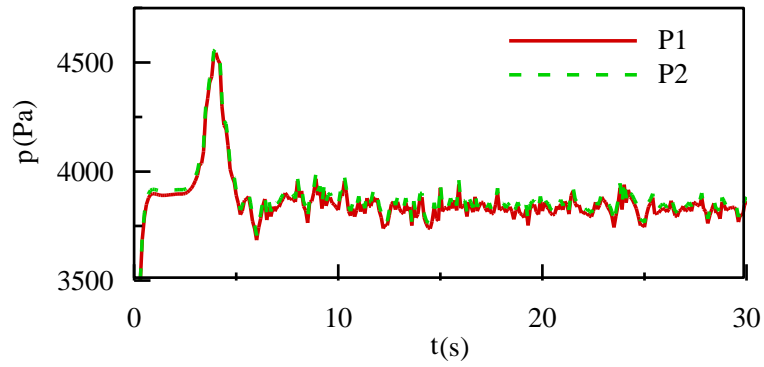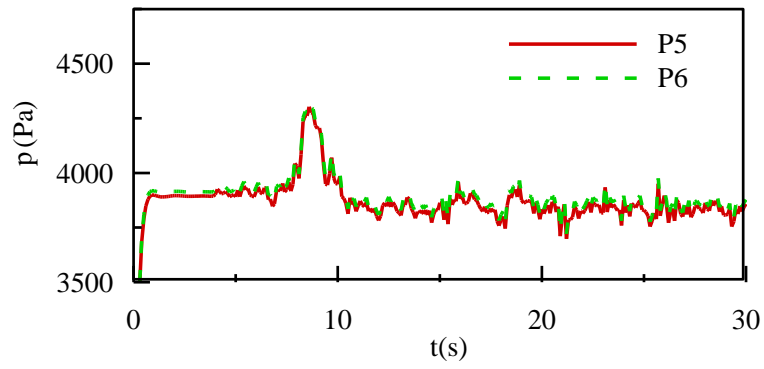
Fig. 4 Time series of dynamic pressure computed at different measurement points
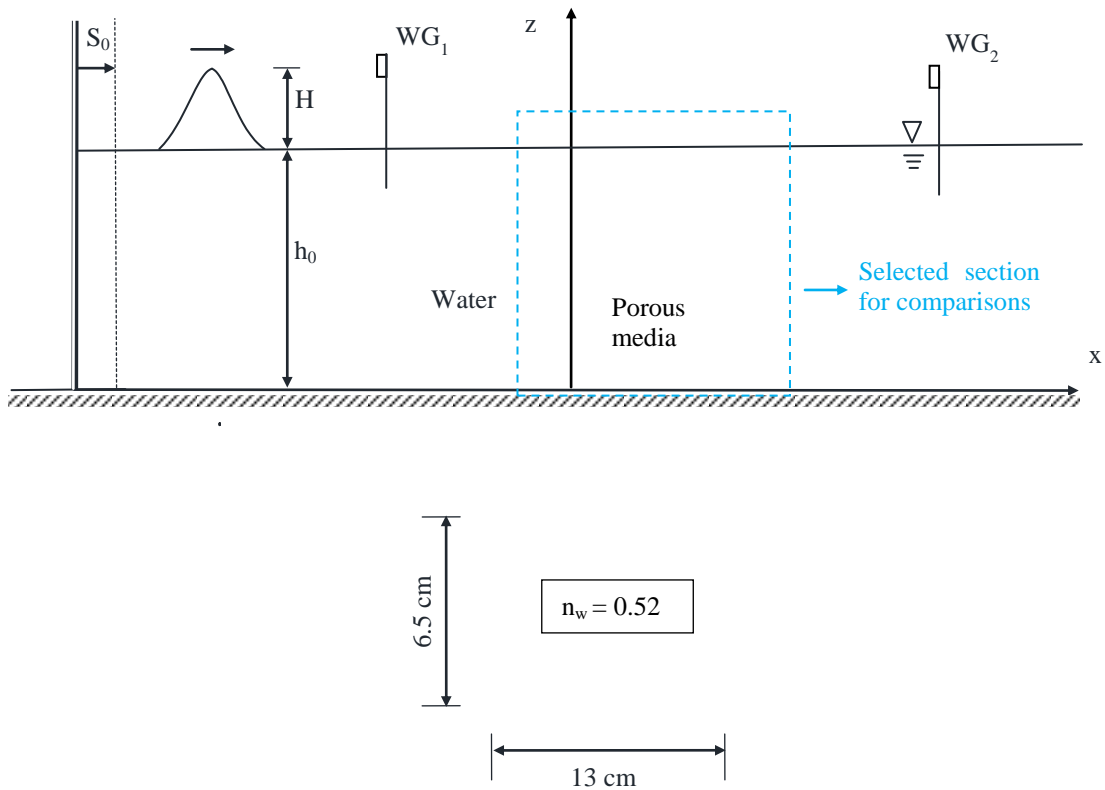
Fig. 5 Schematic diagram of solitary wave propagating over a submerged porous breakwater
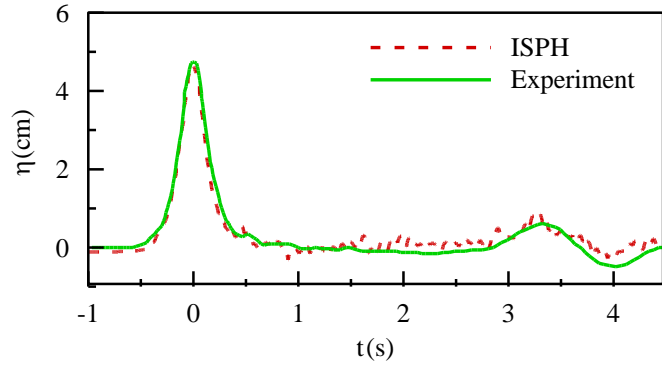
(a)
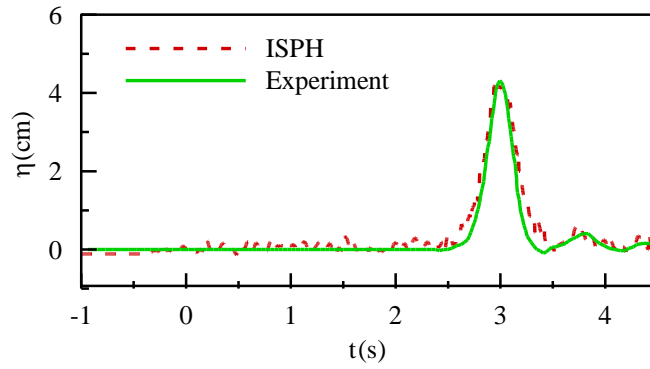
(b)

Fig. 6 Comparison of time series of free surface elevation between ISPH model results and experimental data of Wu and Hsiao (2013) at (a) x = -1.8 m and (b) x = 1.8 m
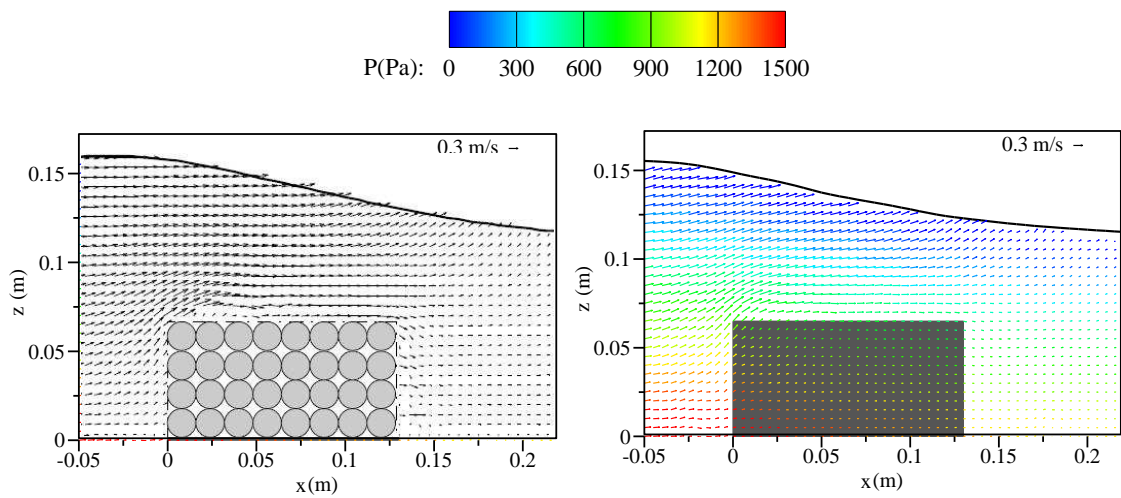
Fig. 7 (a) Comparison of velocity field between model results (right) and experiment (left) at t = 1.45 s
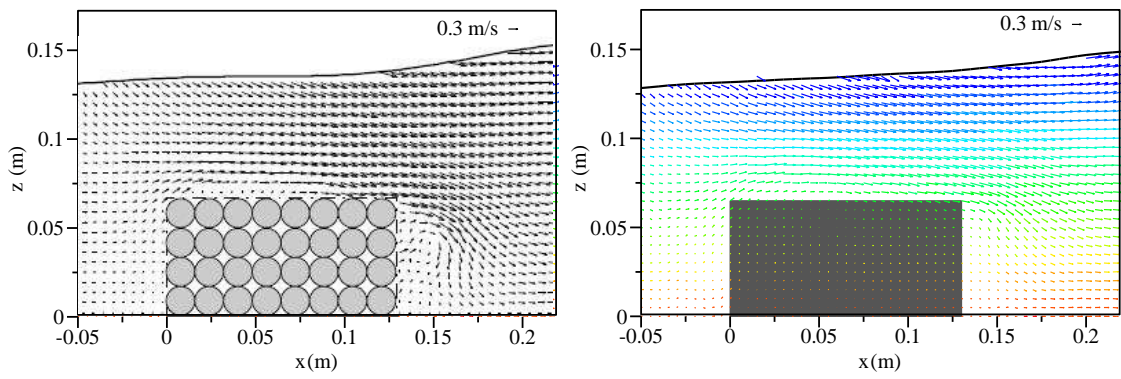
Fig. 7 (b) Comparison of velocity field between model results (right) and experiment (left) at t = 1.65 s
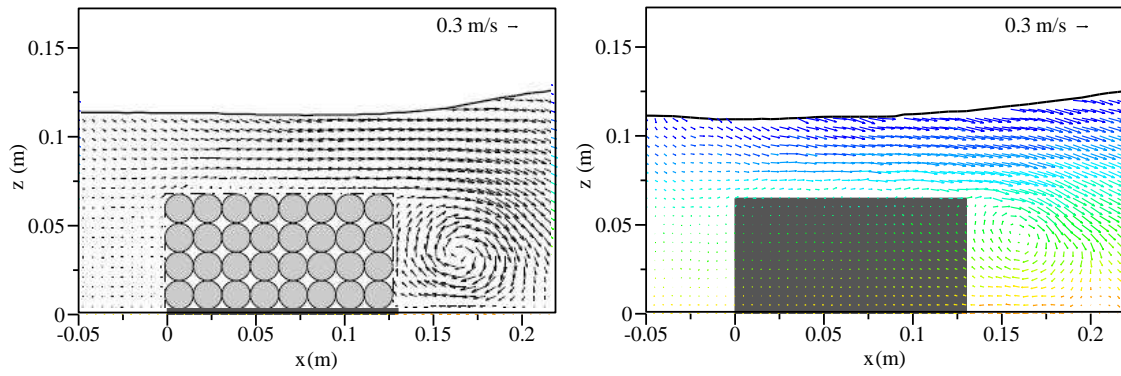
Fig. 7 (c) Comparison of velocity field between model results (right) and experiment (left) at t = 1.85 s
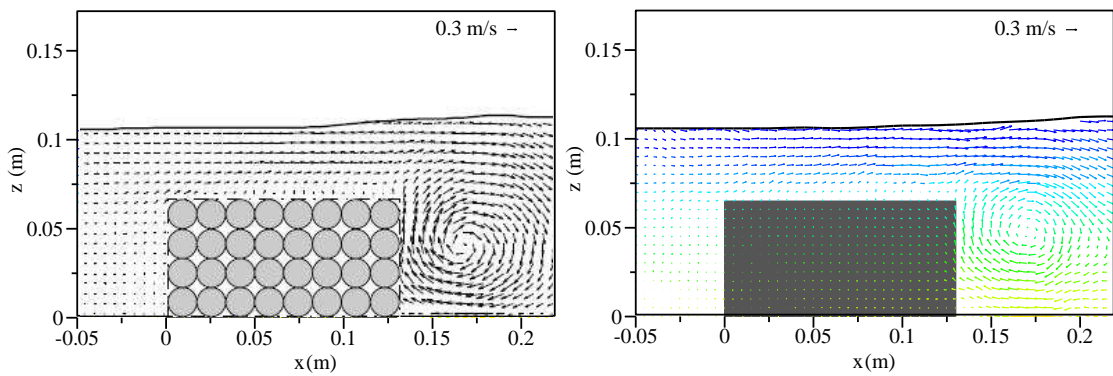
Fig. 7 (d) Comparison of velocity field between model results (right) and experiment (left) at t = 2.05 s
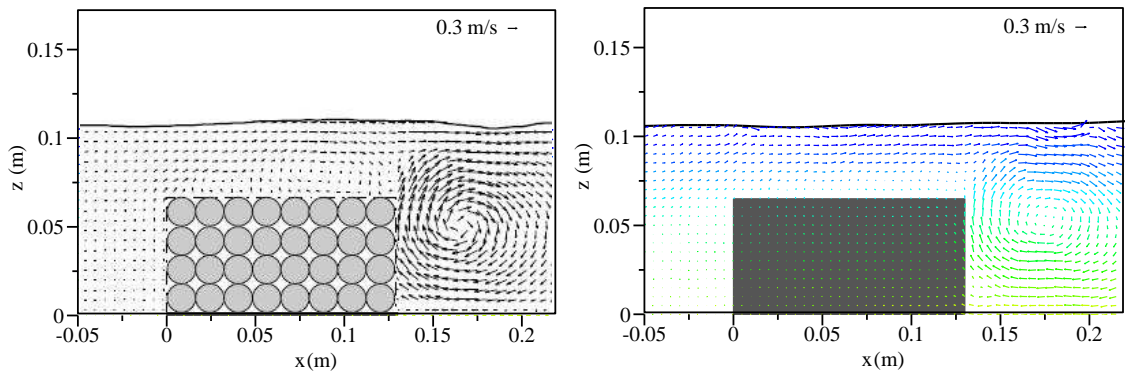
Fig. 7 (e) Comparison of velocity field between model results (right) and experiment (left) at
t = 2.25 s
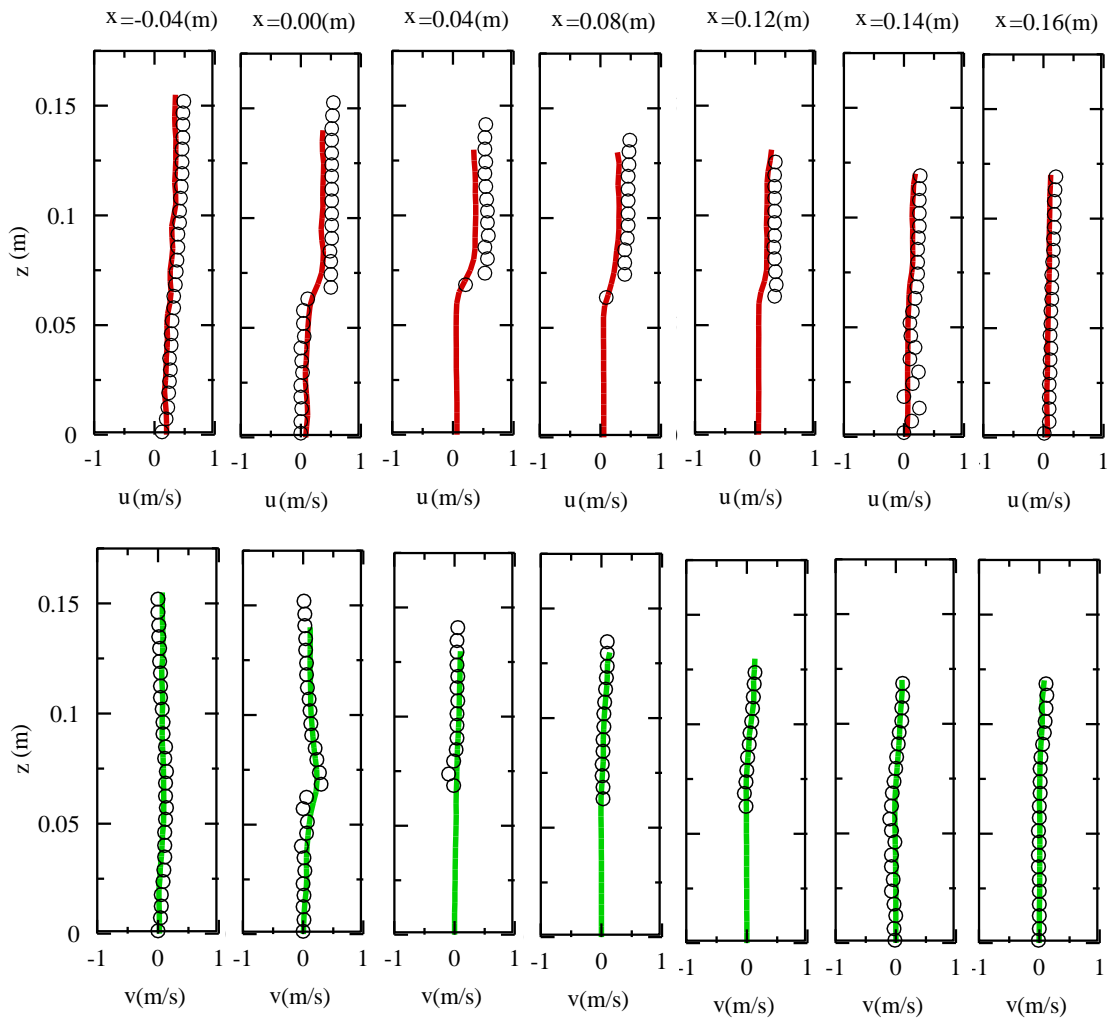
Fig. 8 (a) Horizontal and vertical velocity profiles comparison between model results and
experiment at t = 1.45 s. Circle: experiment; Solid line: ISPH results (red: horizontal velocity,
green: vertical velocity)
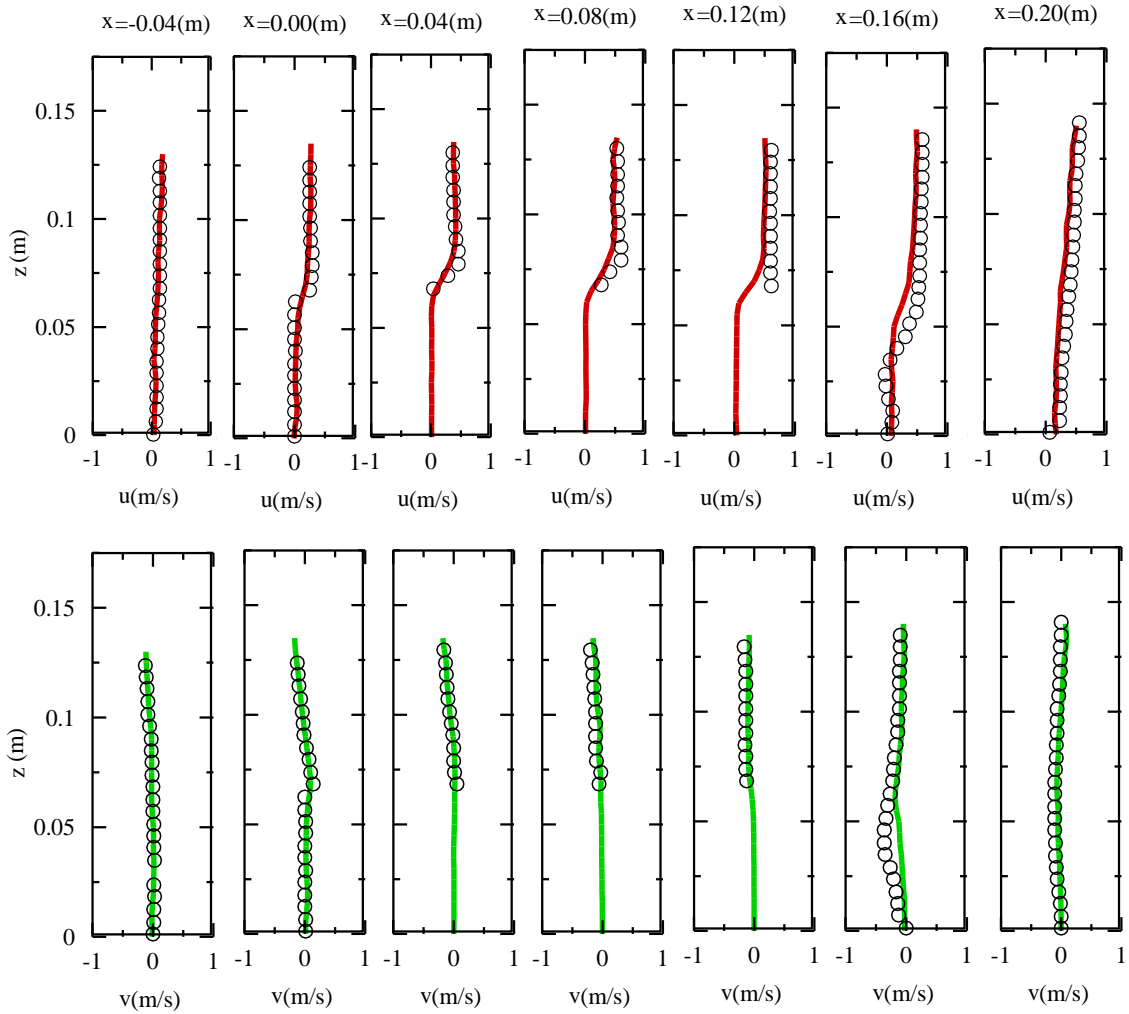
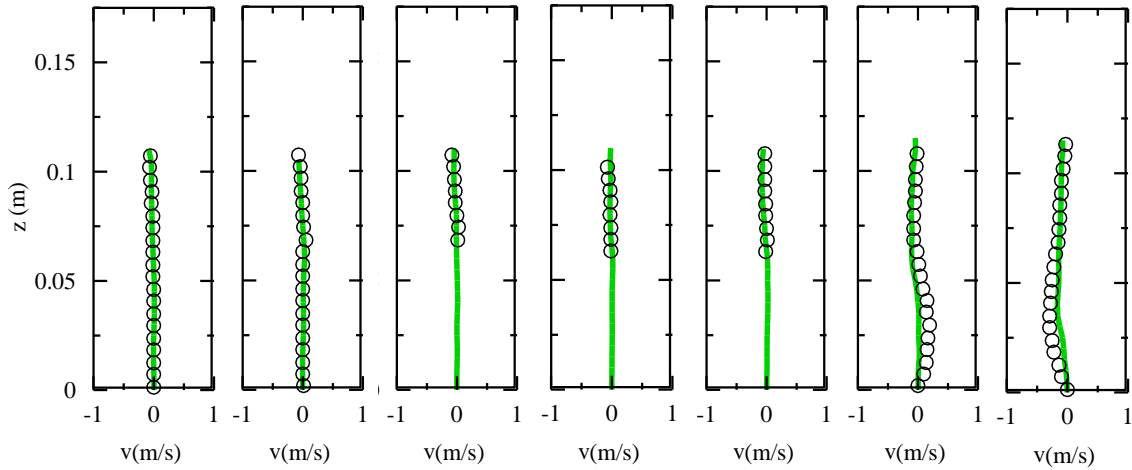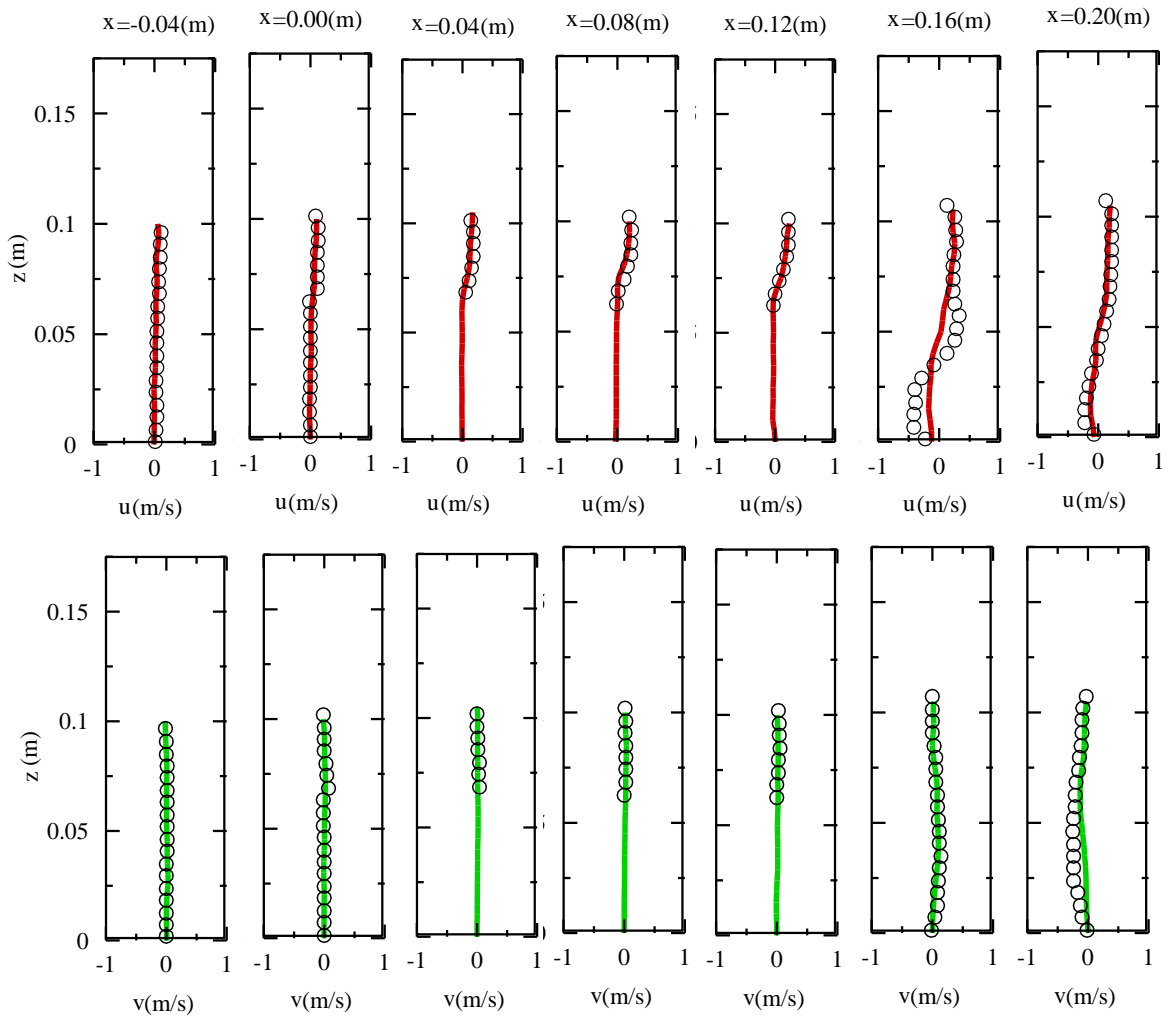Fig. 8 (b) Horizontal and vertical velocity profiles comparison between model results and experiment at t = 1.65 s. Circle: experiment; Solid line: ISPH results (red: horizontal velocity, green: vertical velocity)
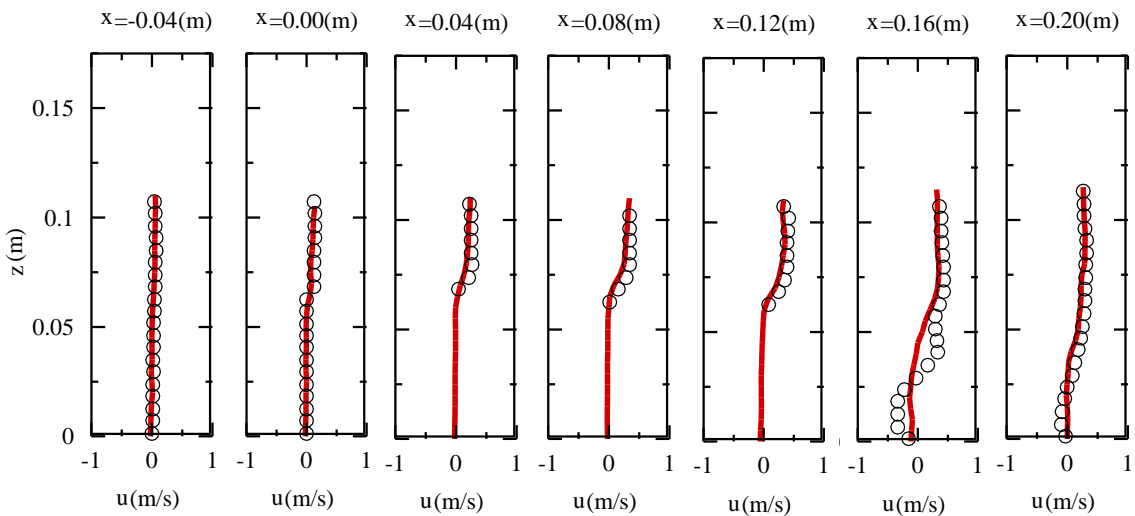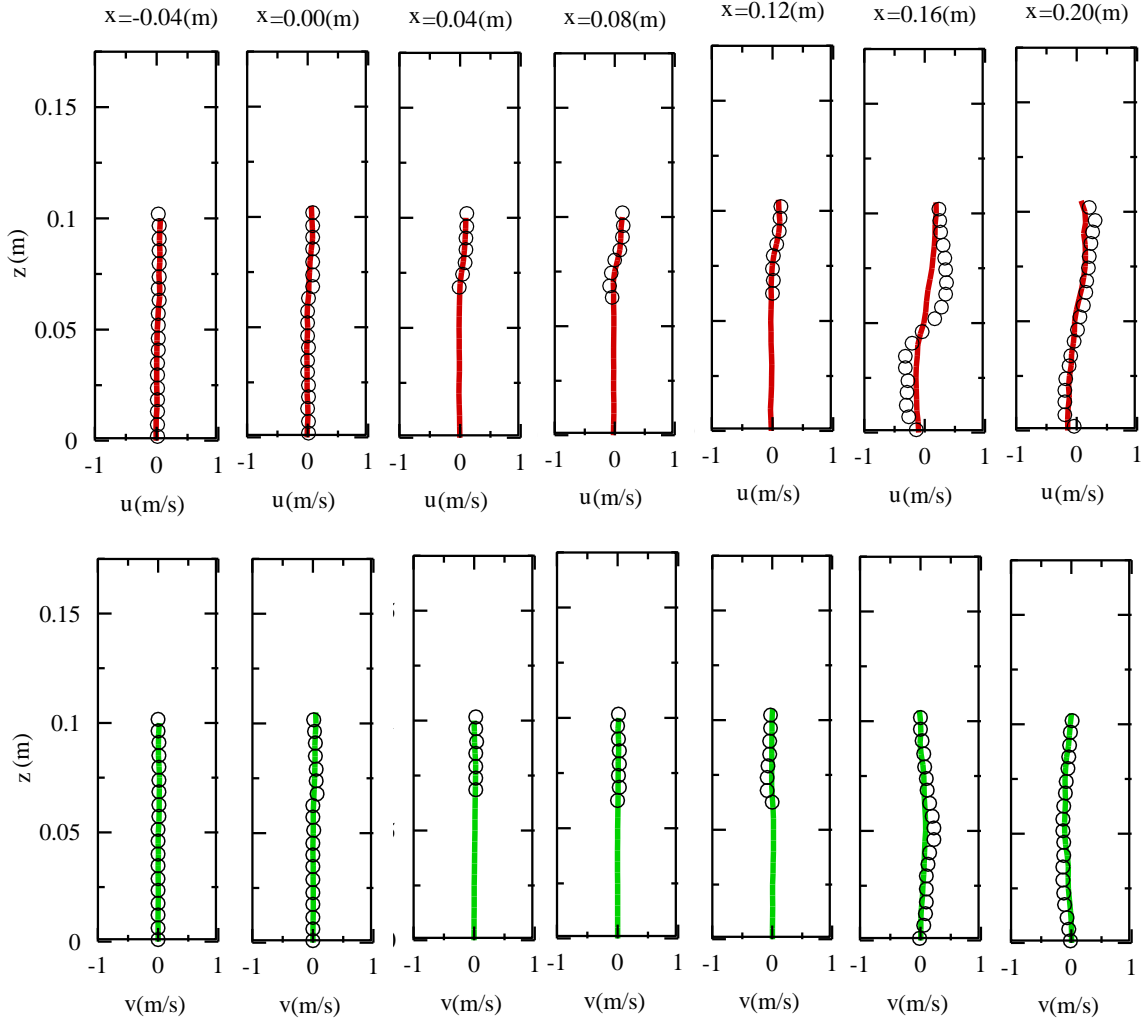
Fig. 8 (c) Horizontal and vertical velocity profiles comparison between model results and experiment at t = 1.85 s. Circle: experiment; Solid line: ISPH results (red: horizontal velocity, green: vertical velocity)


Fig. 8 (d) Horizontal and vertical velocity profiles comparison between model results and experiment at t = 2.05 s. Circle: experiment; Solid line: ISPH results (red: horizontal velocity, green: vertical velocity)

Fig. 8 (e) Horizontal and vertical velocity profiles comparison between model results and experiment at t = 2.25 s. Circle: experiment; Solid line: ISPH results (red: horizontal velocity, green: vertical velocity)

(a)

x=0.08(m)

x=0.08(m)

(b)
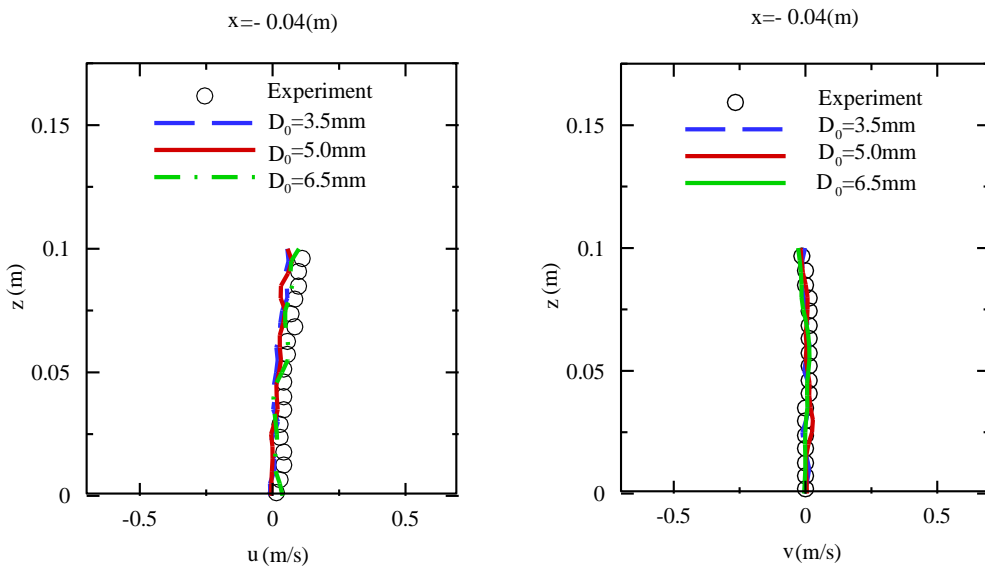
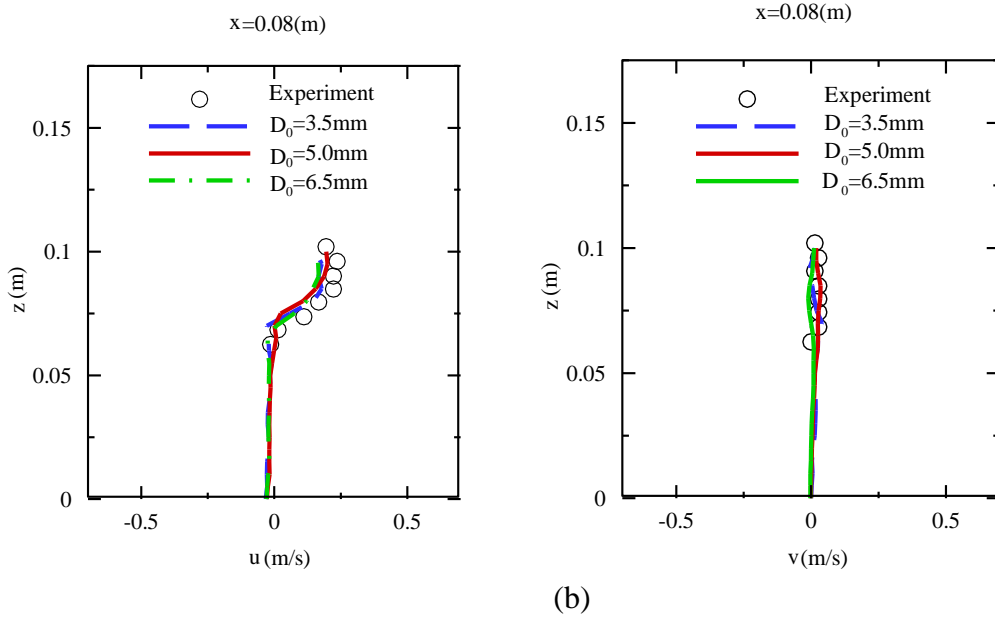Fig. 9 Convergence analysis of ISPH model computations for horizontal (left) and vertical (right) velocity distributions at (a) x = -0.04 m and (b) x = 0.08 m
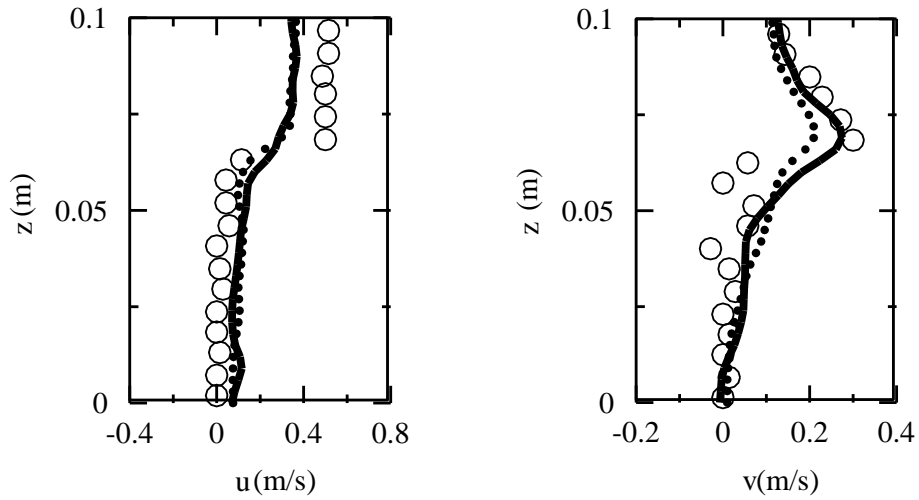

Fig. 10 Horizontal (left) and vertical (right) velocity distributions along depth on weather side of breakwater (Solid line: with interface model; Dotted line: without)